



HAL
open science

A series of Iron(II)-NHC Sensitizers with remarkable power conversion efficiency in photoelectrochemical cells

Anil Reddy Marri, Edoardo Marchini, Valentin Diez Cabanes, Roberto Argazzi, Mariachiara Pastore, Stefano Caramori, Carlo Alberto Bignozzi, Philippe Gros

► To cite this version:

Anil Reddy Marri, Edoardo Marchini, Valentin Diez Cabanes, Roberto Argazzi, Mariachiara Pastore, et al.. A series of Iron(II)-NHC Sensitizers with remarkable power conversion efficiency in photoelectrochemical cells. *Chemistry - A European Journal*, 2021, 27 (65), 10.1002/chem.202103178 . hal-03347445v2

HAL Id: hal-03347445

<https://hal.science/hal-03347445v2>

Submitted on 10 Jan 2022

HAL is a multi-disciplinary open access archive for the deposit and dissemination of scientific research documents, whether they are published or not. The documents may come from teaching and research institutions in France or abroad, or from public or private research centers.

L'archive ouverte pluridisciplinaire **HAL**, est destinée au dépôt et à la diffusion de documents scientifiques de niveau recherche, publiés ou non, émanant des établissements d'enseignement et de recherche français ou étrangers, des laboratoires publics ou privés.

A series of Iron(II)-NHC Sensitizers with remarkable power conversion efficiency in photoelectrochemical cells

Anil Reddy Marri,^[a] Edoardo Marchini,^[b] Valentin Diez Cabanes,^[c] Roberto Argazzi,^[d] Mariachiara Pastore,^{*[c]} Stefano Caramori,^{*[b]} Carlo Alberto Bignozzi^[b] and Philippe C. Gros,^{*[a]}

To Prof. Vincenzo Balzani on the occasion of his 85th birthday

- [a] Dr A. Reddy-Marri, Dr P.C. Gros
Université de Lorraine, CNRS, L2CM,
F-54000 Nancy, France
E-mail: philippe.gros@univ-lorraine.fr
- [b] E. Marchini, Prof. C.A. Bignozzi, Prof. S. Caramori
University of Ferrara
Department of Chemical, Pharmaceutical and Agricultural Sciences,
Via L.Borsari 46, 44121, Ferrara, Italy
E-mail: cte@unife.it
- [c] Dr V. Diez Cabanes, Dr M. Pastore
Université de Lorraine, CNRS, LPCT,
F-54000 Nancy, France
E-mail: mariachiara.pastore@univ-lorraine.fr
- [d] Dr R. Argazzi
University of Ferrara
CNR-ISOF c/o Department of Chemical, Pharmaceutical and Agricultural Sciences
Via L.Borsari 46, 44121, Ferrara, Italy

Supporting information for this article is given via a link at the end of the document.

Abstract: A series of six new Fe(II)NHC-carboxylic sensitizers with their ancillary ligand decorated with functions of varied electronic properties have been designed with the aim to increase the metal-to-surface charge separation and light harvesting in iron-based Dye-sensitized solar cells (DSSCs). **ARM130** scored the highest efficiency ever reported for an iron-sensitized solar cell (1.83%) using Mg²⁺ and NBu₄-based electrolyte and a thick 20 μm TiO₂ anode. Computational modelling, transient absorption spectroscopy and electrochemical impedance spectroscopy (EIS) revealed that the electronic properties induced by the dimethoxyphenyl substituted NHC ligand of **ARM130** led to the best combination of electron injection yield and spectral sensitivity breadth.

Introduction

Transition metal complexes with long-lived excited metal to ligand charge transfer (MLCT) states are ubiquitous in a wide range of photophysical and photochemical applications.^[1–3] In order to develop more sustainable technologies, an important challenge is to replace the scarce noble metals such as Ru, Ir or Pt, representing the current stars in the field, with cheaper and non-toxic first-row metals.^[4]

Due to earth-abundance and low-cost of iron, its complexes have been widely investigated but a too small ligand field splitting energy has limited for a long time their successful application.^[5,6] Recently, introduction of pyridyl-NHC ligands has been shown to notably affect the energy order of the MLCT and metal center (MC) excited-states manifold in iron(II) complexes, thus preventing the detrimental ultrafast excited state relaxation into the quintet ⁵MC state.^[7–10] The MLCT lifetime has increased from tens of picoseconds, for complexes with tridentate C[∧]N[∧]C[∧]^[11–13] and bidentate C[∧]N ligands,^[14,15] to nanoseconds for

compounds bearing tridentate C[∧]C[∧]C[∧] ligands,^[16] thus making iron complexes much more promising for photochemical applications. Our group has reactivated the field of iron-sensitized solar cells (FeSSCs) -asleep since the pioneering works by Ferrere^[5]- in which ruthenium complexes are the gold standards due to their long-lived MLCT state allowing efficient injection into the semiconductor.^[17]

Some of us have reported the first proof of concept of a working FeSSC using the homoleptic complex **C1** (Figure 1) as sensitizer, with albeit a low efficiency.^[18] Working thoroughly on electrolyte and cell engineering allowed to reach 1% efficiency with the same complex, the use of the MgI₂-containing electrolytes notably improved the interfacial charge generation and boosted the photocurrent from 0.4 to 3.3 mA.cm⁻².^[19] This performance was very recently further improved up to the best efficiency of 1.5 % (J_{sc} = 4.8 mA.cm⁻²) ever recorded for a FeSSC by sensitizing the cell with the heteroleptic complex **ARM13** (Figure 1) designed to promote an unidirectional charge transfer and thus an optimized dye-to-TiO₂ electron flow.^[20]

Our recent results clearly show that FeSSC is a promising research area, and that the door is opened to reach higher efficiencies by designing new sensitizers with optimized charge separation while engineering electrolytes and semiconductors adapted to this new generation of sensitizers.

To our knowledge, the impact of the electronic modifications of the ancillary ligand (that will not be bound to TiO₂ in the SSC) in heteroleptic complexes on the photovoltaic properties of the corresponding device has not been investigated yet. To this purpose, six new heteroleptic complexes with ancillary ligands bearing electron withdrawing or donating substituents (Figure 1) have been prepared and successfully used as sensitizers in TiO₂-based FeSSCs. The photophysical, electrochemical and photovoltaic properties of the new complexes were investigated. Herein we report an unprecedented 1.83% record efficiency

combining the **ARM130** sensitizer, Mg^{2+} -based electrolyte and a thick TiO_2 photoanode.

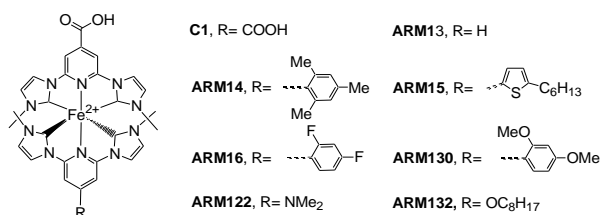
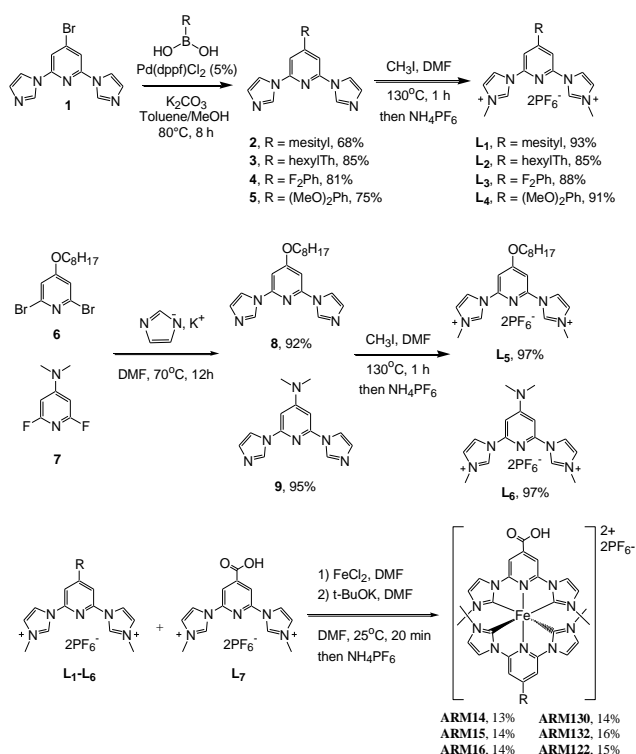


Figure 1. Chemical structures of Fe(II) NHC sensitizers studied in this work, the counter ion is PF_6^- in every case

Results and Discussion

Synthesis of ligands precursors and iron (II) complexes

The pyridyl-NHC ligands to be coordinated to iron required the prior preparation of the corresponding imidazolium salts precursors **L**₁-**L**₆ (Scheme 1). **L**₁, **L**₂, **L**₃ and **L**₄ were obtained in good yields respectively by quaternization of pyridylimidazoles **2**, **3**, **4** and **5** resulting from a Suzuki coupling of the bromo derivative **1**^[20] with the appropriate aryl boronic acids. **L**₅ and **L**₆ were obtained from amination of respectively dibromo and difluoropyridines **6**^[21] and **7**^[22] using potassium imidazolate at 70°C in DMF and final quaternization with methyl iodide.



Scheme 1. Synthesis of ligand precursors and complexes

The target heteroleptic complexes were obtained using a one-pot synthesis by reacting FeCl_2 with an equimolar mixture of the

appropriate ligand **L**₁-**L**₆ with **L**₇,^[23] bearing the carboxylic function, in the presence of *t*-BuOK as the base.

Spectroscopic properties of complexes

The UV-Vis absorption spectra of all the six new complexes in methanolic solution are shown in Figure 2 and the data concerning the lowest energy bands are collected in Table 1, along with the calculated lowest-energy vertical excitation energies, their oscillator strengths and their main singly excited configurations composing the electronic excitation. The simulated absorption spectra are displayed in Figure S45 in ESI. All the complexes displayed three distinct absorption bands. The band at higher energy (250-350 nm) is assigned to π - π^* transition, while the two other bands, in the lower energy region, correspond to the Fe-carbene MLCT transitions (340-440 nm) and Fe-Pyridine MLCT transitions (410-600 nm).

Focusing on the lowest-energy portion of the spectrum, the MLCT Fe-Pyridine band, the four aryl tethered complexes **ARM14**, **ARM15**, **ARM16** and **ARM130** present a broad and intense absorption, ranging from 410 to 600 nm while **ARM122** and **ARM132** (N,N-dimethylamino donor and O-Octyl on the pyridine) absorbed in a narrower window (450-600 nm). Among all, **ARM15** showed the broadest and most red shifted absorption with the highest molar extinction coefficients (501 nm, 25228 $\text{M}^{-1}\cdot\text{cm}^{-1}$) due to the extension of π -conjugation promoted by the thiophene unit.

Heteroatom-substituted complexes **ARM122** and **ARM132** showed slightly different behavior i.e., the two MLCT bands (Fe-Py and Fe-Carbene) were found of similar intensities unlike the other complexes, due to the strong donating capability (due to lone pair of electrons) from N,N-dimethylamino and O-Octyl groups. These two complexes displayed lower ϵ values at lower energy domain (12447 $\text{M}^{-1}\text{cm}^{-1}$ at 489 nm, for **ARM122** and 11459 $\text{M}^{-1}\text{cm}^{-1}$ at 498 nm, for **ARM132**).

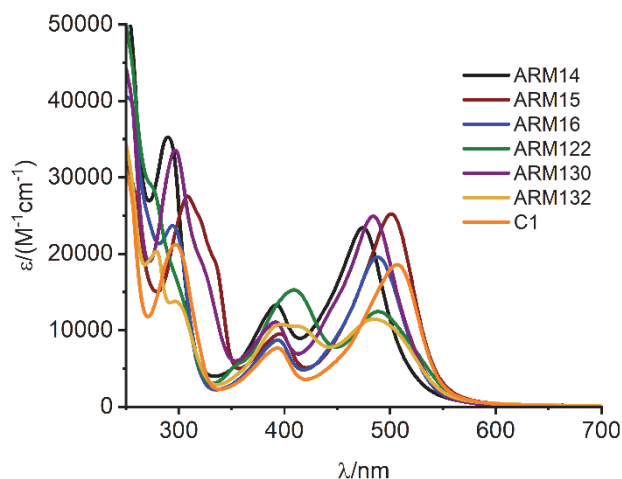


Figure 2. UV-Vis spectra of Fe(II)NHC Complexes in MeOH

In this context, TD-DFT calculations were performed to shed light on the main characteristics of the lowest energy MLCT absorption bands which have been discussed above. Although a systematic slight blue-shift of ca. 0.2 eV is obtained, in analogy with our previous results,^[20] the main trends in the absorption features are consistently reproduced by our calculations (Figure S45).

Table 1. Experimental absorption maxima in MeOH and on TiO₂, calculated vertical excitation energies with relative oscillator strengths and nature of the main single particle excitations contributing to these excited states (percentage for each transition). All energy values are in nm.

Dye	Experiments		Theory	
	λ_{\max} (nm) ($\epsilon \cdot 10^4 \text{ M}^{-1} \text{ cm}^{-1}$)	λ_{\max} (nm) (TiO ₂)	E_{exc} (nm) (oscillator strength)	Transition (%)
ARM13	507 (1.85)	478	461 (0.15)	H-2→L (63.4%)
ARM14	474 (2.35)	500	464 (0.20)	H-2→L (63.8%)
ARM15	501 (2.52)	500	470 (0.43)	H-2→L (60.6%)
ARM16	488 (1.96)	482	464 (0.27)	H-2→L (63.4%)
ARM122	489 (1.24)	490	475 (0.18)	H-2→L (63.5%)
ARM130	484 (2.49)	486	469 (0.30)	H-2→L (63.4%)
ARM132	485 (1.14)	498	467 (0.16)	H-2→L (63.5%)

In particular, **ARM14**, **ARM15**, **ARM16** and **ARM130** displayed larger MCLT absorption band intensities (oscillator strengths larger than 0.2) with respect to **ARM122** and **ARM132**, with **ARM15** being the one showing the most intense absorption. To analyse the nature of the HOMO-2→LUMO transition, composing the lowest energy MLCT band, we have carried out a Natural Transition Orbital (NTO) analysis,^[24] which provides insights on the topology of the excited state (see Figure S46). Notably, all the dyes showed an identical delocalization, for both holes and electrons, to the one displayed by the unsubstituted **ARM13** reference dye, thus evidencing the negligible role played by the chemical substitution in the nature of the MCLT band. For a more quantitative estimation of the hole/electron localization on the different molecule moieties, we analysed the transition density matrix by using the TheoDORÉ package.^[25] The results are collected in Table S2, where the values calculated for the reference homoleptic (**C1**) and unsubstituted heteroleptic (**ARM13**) are also shown. As already evidenced by the NTOs, globally the presence of the substituent (SG) on the non-anchored ligand (NHC_{top}) does not significantly modify the charge transfer properties. Overall, upon excitation, about 72-75% of the hole is localized on the Iron center and 12-18% on the ligand bearing the carboxylic group (NHC_{bot}), while less than 1% is on the NHC_{top}. Concerning the electron, the largest fraction is still localized on the NHC_{bot} (60-70%), with a small fraction (14-16%) reaching the anchoring group. The substituent group is generally not involved in the transition. Within the series of dyes, **ARM15** presents the less efficient and unidirectional CT: a small fraction of the electron (ca. 13%) is indeed localized on the non-anchored NHC_{bot} ligand, and a reduced amount of charge reaches the anchoring group, thus the TiO₂ substrate. Based on these results, we may therefore expect a less efficient TiO₂ sensitization by **ARM15** despite its intense and red-shifted absorption (Figure 2)

Spectroscopic and Electrochemical properties of Fe(II) sensitized thin films.

In order to optimize the photon to electron conversion of these new dyes, $\approx 16 \mu\text{m}$ transparent thick films have been prepared and preliminarily sensitized with a first set of dyes consisting of **ARM16**, **ARM122**, **ARM130**. These were compared with the standard homoleptic **C1** complex. The recorded absorption spectra of the dye-sensitized $16 \mu\text{m}$ TiO₂ films are reported in Figure 3a.

All these spectra are characterized by an intense MLCT band centered around 500 nm that, at the λ_{\max} harvests $\geq 99\%$ of the incident light for all the selected compounds. The average dye surface loading Γ , calculated according to eq.1, where A and ϵ are the maximum visible absorbance and molar extinction coefficient of each dye, is very similar among the three different heteroleptic complexes (average value $0.110 \pm 0.020 \mu\text{mol cm}^{-2}$, Table S3) and comparable with that of the standard homoleptic **C1** dye.

$$\Gamma = \frac{A(\lambda)}{1000\epsilon(\lambda)} \quad (\text{eq. 1})$$

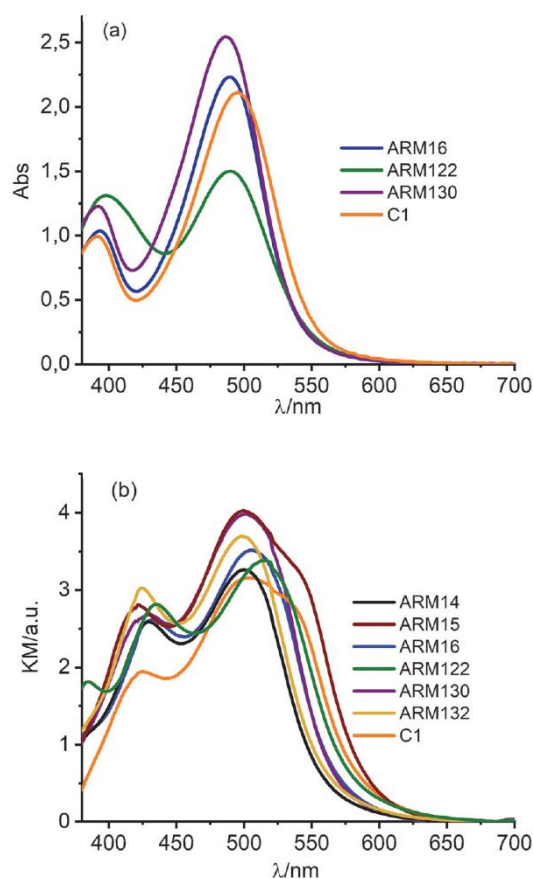


Figure 3: (a) Absorption spectra for some selected Fe(II)NHC complexes loaded on $16 \mu\text{m}$ TiO₂ recorded against an identical undyed electrode as a reference. (b) Absorption spectra for the Fe(II)NHC sensitized TiO₂ recorded in diffuse reflectance mode (illumination was through the FTO back contact) and reported in KM units.

Despite the good absorbance at the MLCT maximum the absorption spectra of the sensitized films remain relatively

narrow, consistently with the spectral features of the NHC dyes, causing the harvesting to fall off significantly for $\lambda > 550$ nm. We have thus decided to improve the harvesting by preparing thicker TiO₂ films (three transparent layers having a total thickness of ca. 20 μm equipped with a scattering overlayer (Solaronix Ti-nanoxide R/SP > 100 nm). The UV-Vis spectra of these films generally show a broadened main visible band which significantly extends the spectral sensitization to longer wavelengths. All dyes manifest, indeed, their maximum harvesting between 500 and 550 nm while the best absorber is **ARM15** whose absorption extends up to 650 nm (Figure 3b).

The thermodynamic properties of our Fe(II)NHC based complexes have been investigated by cyclic voltammetry of TiO₂ or ZrO₂ sensitized thin films immersed in 0.1 M LiClO₄/CH₃CN (Figure 4) and are summarized in Table 2. We found this experiment of importance to account for the perturbation induced on the dye levels by adsorption on the semiconductor surface. ZrO₂ was used as an electrochemically inert porous support^[26–28] in order to explore the energetics of dye reduction, whose observation would be precluded on titania films owing to conduction band reduction occurring at lower potentials. The observation of electrochemical process on ZrO₂ is however still possible due to charge hopping between adjacent dyes, mediated by species electronically coupled with the FTO ohmic contact. The anodic scan (Table 2) reveals quasi-reversible Fe(II)/(III) waves ($\Delta E \approx 80/100$ mV) whose $E_{1/2}$ ranges from ca. 0.5 V vs SCE (**ARM-122**) to ca. 0.7 V Vs SCE (**ARM14**). In general, these processes are fully consistent with those observed on ZrO₂ films as well, where however, in some cases a cathodic shift of ca. 50 mV is observed. From the study of the Fe(II)/(III) process we can conclude that these FeNHC complexes are endowed with a relatively fast electron transfer kinetics and that the influence of the group at the 4 position of the pyridine on the Fe(II)/(III) energetics is quite evident. We observe the most positive potentials (from 0.70 to 0.69 V vs SCE) with functionalized benzene or thiophene rings (**ARM14** > **ARM16** > **ARM15**), particularly when modified with electron accepting substituents.

The presence of donor groups like –OR either as substituents of the benzene ring (**ARM130**, 0.64 V vs SCE) or directly attached to the pyridine (**ARM132**, 0.65 V vs SCE) causes a cathodic shift of ca 50 mV with respect to the previous series. The less positive oxidation potential is found when a stronger electron donor like dimethylamine is directly bound to the NHC ligand (**ARM122**, 0.49 V vs SCE). For all cases the regeneration of Fe(II) by the iodide/iodine couple in the electrolyte is an exergonic process in the order of 150-300 meV. Such a driving force should guarantee a fast electron donation by the redox couple. All these Fe(II) complexes exhibit a similar irreversible, multi-electronic cathodic wave peaking at ca. -1.5 V vs SCE. The energy difference between the anodic and cathodic processes observed on the ZrO₂ adsorbates agrees well with the onset of the absorption spectrum of the sensitized thin films, affording an estimate of the spectroscopic energy (E^{00}) and indicating that the spectroscopic states are energetically related with the electrochemical states, confirming the metal to ligand charge transfer nature of the main visible band of all these NHC complexes. Finally, from the estimated E^{00} and Fe(II)/(III) $E_{1/2}$ we can evaluate the lowest excited state potential of these dyes ($E^{*ox} = E_{1/2} - E^{00}$). The driving force for charge injection ($\Delta G_{inj} = -e(|E^{*ox}| - |EFB|)$), where EFB is the flat band potential of TiO₂)

is thus in all cases quite substantial, being in the order of at least -0.8 eV, using the commonly accepted value of -0.7 V vs SCE for the flat band of TiO₂ in the presence of a lithium containing organic solvent like acetonitrile^[29,30]. Thus, thermodynamic limitations involving the key electron transfer events at the basis of interfacial photoinduced charge separation can be excluded.

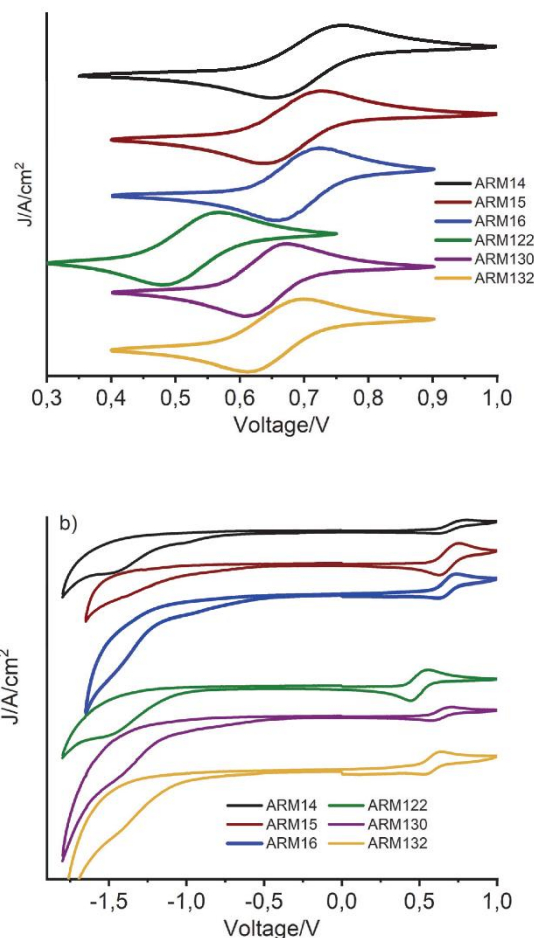


Figure 4: Cyclic voltammeteries recorded on Fe(II)NHC on (a) TiO₂ (anodic scan) and on (b) ZrO₂ (full scan) in 0.1 M LiClO₄/CH₃CN solution

Table 2: Electrochemical parameters for the Fe(II)NHC sensitized TiO₂ or ZrO₂

Dye	$E_{1/2}^{Ox}$ (TiO ₂)/V	$E_{1/2}^{Ox}$ (ZrO ₂)/V	$E_{peakRed}$ (ZrO ₂)/V	$E_{ox} - E_{red}$ CV(ZrO ₂)	E^{00}_{abs} (TiO ₂)
ARM14	0.705	0.706	-1.55	2.25	2.09
ARM15	0.682	0.691	-1.45	2.14	2.09
ARM16	0.691	0.678	-1.49	2.17	2.11
ARM122	0.524	0.494	-1.55	2.04	2.05
ARM130	0.641	0.638	-1.51	2.15	2.10
ARM132	0.654	0.585	-1.48	2.06	2.04

Time resolved spectroscopy

When the Fe(II) sensitized titania films are in contact with small and high-density cations such as Li⁺ (Figure S47), a bathochromic shift is observed, ostensibly due to Stark effect induced by the absorption of these cations on the TiO₂ surface.^[29] Regeneration and recombination kinetics within this sensitizer series have been investigated using transient absorption spectroscopy in the μs -s range. All the reported transient absorption spectra (TAS) (Figure S48) can be

described similarly: the 532 nm excitation of the stained titania film in contact with 0.1 M Li⁺ in acetonitrile, resulted in a strong and long lived (hundreds of ms) ground state bleaching band centered around 500 nm, whose formation is within the instrumental time response (FWHM ca. 7 ns) of the spectrometer. Such feature perfectly mirrors the MLCT manifold of the ground state when the sensitized films are in contact with a Li⁺ containing electrolyte (Figure S47) and is consistent with the photoinduced formation of Fe(III) following charge injection. The ground state bleaching is followed by a weak and featureless absorption band extending in the 600-740 nm region, arising by a combination of spectroscopic contributions from LMCT states and from electrons photoinjected and trapped in the TiO₂ substrate. These spectroscopic features persist for hundreds of ms.

To probe the recombination dynamics and to try to extrapolate a time constant, we have focused on the 500 nm kinetics by exploring the μ s/s time domain in the presence of an excitation energy of 400 μ J/cm²/pulse. Within the above specified time domain, the 500 nm oscillographic traces could be suitably amplified to optimize the signal-to-noise ratio (S/N) by using either 10 k Ω or 1 M Ω impedance pre-amplifiers (Figure 5a). Owing to the inherent inhomogeneity of the nanostructured titania films, recombination kinetics have a complex behavior requiring the fitting of the fastest part of the decay (ca. 50% of the total amplitude) with a power law function,^[31] (See for example fitting in Figure S49) (eq.2), owing to bimolecular electron/hole recombination events occurring at the earliest times. The remaining part of the decay which extends well into the hundred ms time scale was fitted with a stretched exponential function^[32,33] (eq.3) which accounts for the energy distribution of semiconductor/electrolyte states that lead to different recombination rate constants, caused essentially by detrapping of electrons from localized surface states close to the conduction band edge:

$$\Delta A_{t < 2ms} = A + bt^{-c} \quad (\text{eq. 2})$$

$$\Delta A_{t > 2ms} = A' + b'e^{-\left(\frac{t}{\tau}\right)^d} \quad (\text{eq. 3})$$

In equation 3, the d parameter is close to 0.5 for all the different kinetics.^[33] The new dye series show a lifetime in the range of 100-200 ms, significantly longer than the reference **C1** dye whose recovery by recombination is complete on the scale of 100 ms. Nevertheless, these differences in recombination rate are relatively unimportant considering that when the sensitized films are exposed to the I⁻ containing electrolyte (0.1 M LiI, 0.6 M PMII, 0.1Mgl₂, 0.1 M GuNCS, 0.1M TBAI) regeneration occurs within the time resolution of the spectrometer amplified with a 10 k Ω impedance (base width 4 μ s, FWHM 1.5 μ s) (Figure 5b). The slowest regeneration was observed with **ARM122** appearing to be complete on the 0.1 ms time scale, consistent with its lower driving force for iodide oxidation.

For this latter case we can estimate a regeneration time constant of the order of 30 μ s. All dyes, show, more or less evidently, the long lived Stark absorption^[29,30,34] arising from electron accumulation in the sensitized film, no longer compensated by holes localized on the dye sensitizers. The time evolution of this spectroscopic feature is convolved with the instrumental response of our apparatus and sets an upper limit for the regeneration time constant (< 4 μ s). This results in a nearly unitary regeneration efficiency η_{reg} expressed as eq.4 :

$$\eta_{reg} = \frac{k_{reg}}{k_{rec} + k_{reg}} \quad (\text{eq. 4})$$

In equation 4, k_{reg} is the pseudo first order rate constant for the regeneration of the oxidized dye in the presence of electrolyte and is in the order of 10⁶ s⁻¹ for all the species, while k_{rec} represents the rate constant of the recombination process, which is well in the range 10²-10³ s⁻¹. This leads to $k_{reg} \gg k_{rec}$ and to $\eta_{reg} \approx 1$.

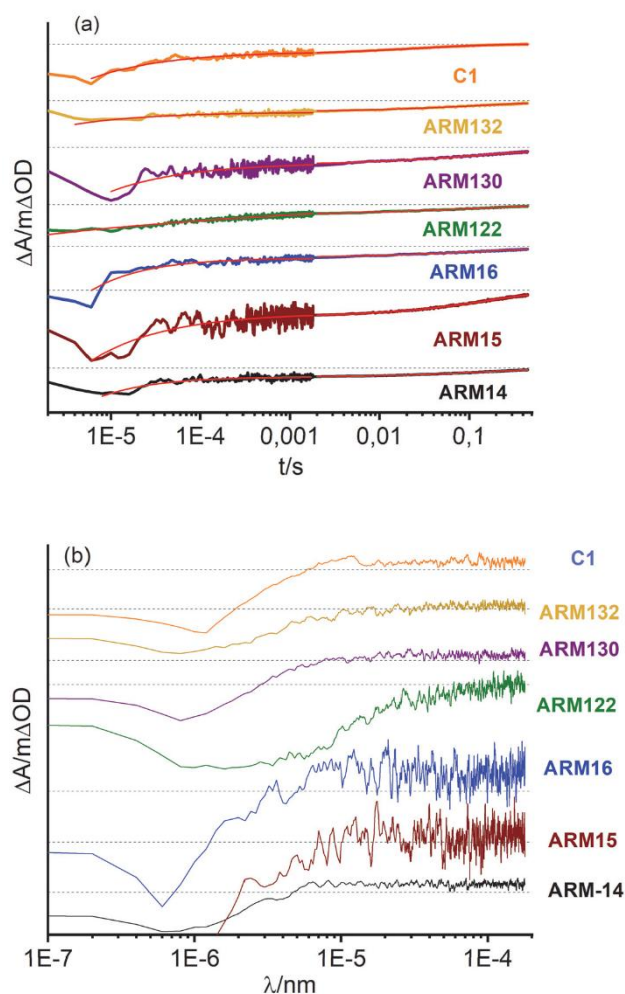


Figure 5: (a) Recombination kinetics recorded at 500 nm for the different complexes obtained by joining traces recorded with 10 K Ω and 1 M Ω input impedances. Laser power: 400 μ J/cm²/pulse. Thin films were in contact with 0.1 M Li⁺/ACN. (b) Regeneration kinetics recorded at 500 nm for the Fe(II)NHC complexes in contact with the reduced form of electrolyte (0.1 M LiI, 0.6 M PMII, 0.1Mgl₂, 0.1 M GuNCS, 0.1M TBAI). Input impedance: 10 K Ω .

Photoelectrochemistry

The power conversion efficiency of a series of DSSC sensitized with this new series of Fe(II)NHC complexes was evaluated with the MgI₂/TBAI based electrolyte that was reported in a previous contribution (0.1 M LiI, 0.6 M PMII, 0.1 M I₂, 0.1 M MgI₂, 0.1 M GuNCS, 0.1 M TBAI in acetonitrile).^[29] The adsorption of high charge density cations like Li⁺ and Mg²⁺ emphasizes the directionality of the MLCT states, and increases the electronic coupling between the dye and the semiconductor conduction band states,^[20] leading to a better charge injection into the semiconductor substrate while the addition of TBAI is

instrumental in decreasing cell resistance by increasing further iodide concentration without further lowering the TiO₂ flat band potential. Initially, three selected dyes, **ARM16**, **ARM122** and **ARM130** were tested with 16 μm TiO₂, showing an incident photon to current conversion efficiency (Figure S50a) ranging from 45% for **ARM122** to over 60% for **ARM130**. Among the explored series, this latter displays the best combination of high IPCE and light harvesting, leading to an integrated short circuit photocurrent density (J_{sc}) of ca. 6 mA/cm² that is in good agreement with the J_{sc} obtained under white light (Figure S51). We note that the integrated J_{sc}, arising from monochromatic measurements is slightly higher than that recorded under white light, probably due to some diffusional limitations when the cell is simultaneously exposed to the entire AM1.5G spectrum. Correction of the IPCE for the LHE terms, affords the Absorbed Photon to Current Conversion Efficiency (APCE % = Φ_{inj}·η_c) which is substantially wavelength independent and reaches a maximum value of ca. 55-60%. Since, η_c, the efficiency of electron collection at the counter electrode, is related to the regeneration of the oxidized dye (assuming recombination with I₃⁻ to be a negligible loss pathway under weak monochromatic illumination), that was demonstrated to be practically unitary by time resolved measurements, we find that maximum injection quantum yield (Φ_{inj}) of ca 50% appears to be the main limiting factor of Fe(II)NHC based DSSCs. Overall J/V curves under AM1.5 G afford power conversion efficiencies (PCE %) of 1.43 %, 1.24 %, 1.10 % and 0.91 % for **ARM16**, **C1** and **ARM122** respectively (Table S5). A further enhancement was obtained by adding a scattering top layer that helps to increase the optical path of photons in the nanostructured titania films, achieving a better harvesting at those longer wavelengths which are poorly absorbed by the sensitizers. This leads to a broader IPCE (Figure S52a) and to an integrated J_{sc} of 7 mA/cm².

Under white light (Figure S52b), the PCE% trend **ARM130**>**ARM16**>**C1**>**ARM122** was maintained with a general improvement in the efficiency (Table S6). **ARM130** exhibited a J_{sc} of 6.33 mA/cm², a Voc of 0.46 V and an overall efficiency of 1.65%. Owing to the good regeneration efficiency which should result in negligible recombination and long diffusion length for the photoinjected electrons, the thickness of the transparent active TiO₂ layer was further increased to ca. 20 μm, while a light scattering overlayer was added in order to increase the optical path of the photons striking the sensitized film. This photoanode configuration was then extended to the whole Fe(II)NHC series (Table 3). Figure 6a reports the IPCE spectra together with the integrated photocurrent density. We observe that, compared to the action spectra reported in Figure S50a, the use of thicker titania films combined with the scattering, extends the photoconversion threshold slightly beyond 700 nm. In agreement with the diffuse reflectance spectra of Figure 3, the largest photoconversion is observed in the 450-650 nm interval which is coincident with the MLCT absorption of these species. In most cases the maximum IPCE values were found in the 50-60% range, with top levels for **ARM15** and **ARM130**. This latter reaches an IPCE peak of ca. 60% at 570 nm, affording a photocurrent of ca. 7 mA/cm² owing to its best combination of spectral sensitivity and charge injection yield.

The trend in the action spectra was confirmed by J/Vs (Figure 6b) where **ARM130** showed the best combination of J_{sc} (ca. 7 mA/cm²) and Voc (0.47V) leading to a power conversion efficiency (PCE %) of 1.83%. This, to the best of our knowledge,

represents the best conversion efficiency ever reported to date for a FeSSC.

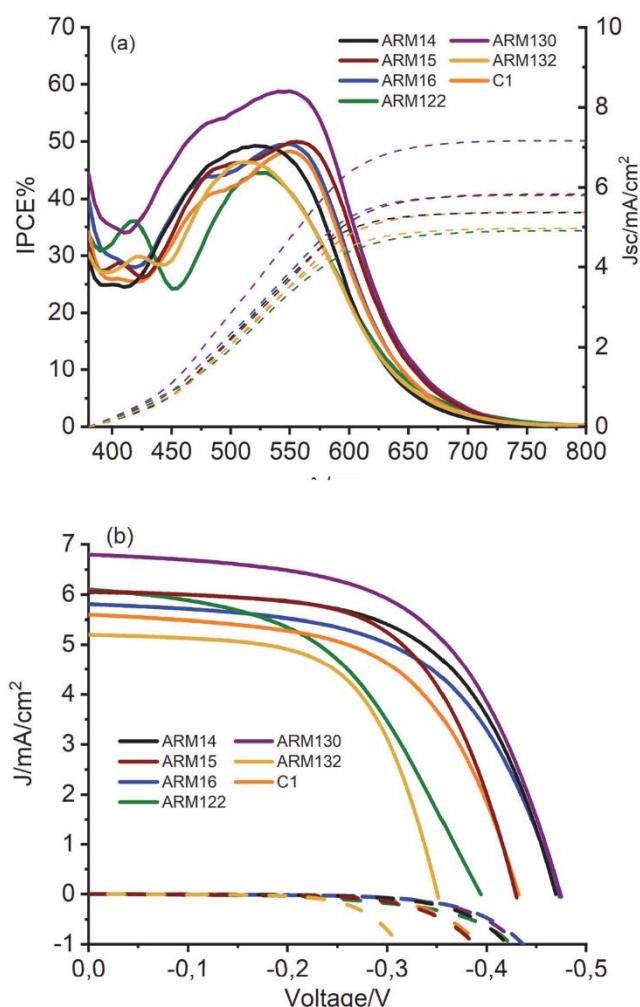


Figure 6: (a) Incident photon to current conversion efficiency (IPCE) spectra recorded for Fe(II)NHC based DSSCs and their relative integrated photocurrent (dotted lines). (b) Photocurrent density-Voltage (J/V) curves recorded for the different Fe(II)NHC complexes in the presence of 0.1 M LiI, 0.6 M PMII, 0.1 M I₂, 0.1 M MgI₂, 0.1 M GuNCS, 0.1 M TBAI in acetonitrile. Cells were composed with a photoanode ca. 20 μm thick TiO₂ plus a scattering layer.

Table 3: Efficiency parameters recorded for Fe(II)NHC sensitized 20 μm TiO₂ and equipped with a top scattering layer

Dye	J _{sc} /mA/cm ²	Voc/V	FF%	PCE%
ARM14	6.03±0.34	0.47±0.01	59±1	1.68±0.14
ARM15	6.07±0.45	0.43±0.01	61±3	1.58±0.13
ARM16	5.81±0.41	0.47±0.01	57±3	1.56±0.18
ARM122	6.11±0.46	0.39±0.01	49±2	1.17±0.15
ARM130	6.80±0.17	0.47±0.02	57±1	1.83±0.10
ARM132	5.20±0.33	0.35±0.01	61±2	1.11±0.12
C1	5.60±0.29	0.44±0.01	56±1	1.39±0.13

Electrochemical impedance spectroscopy (EIS)

To gain a deeper insight into the photoelectrochemical behavior of the FeSSCs, the electrochemical impedance response of the cells under AM 1.5G illumination has been explored. The sampling of the J/V curves at forward voltages along the descending branch of each J/V characteristic has been

performed. Typically, voltage values between the open circuit photovoltage up to -0.25 V (onset of the plateau region of the J/V s) were sampled.

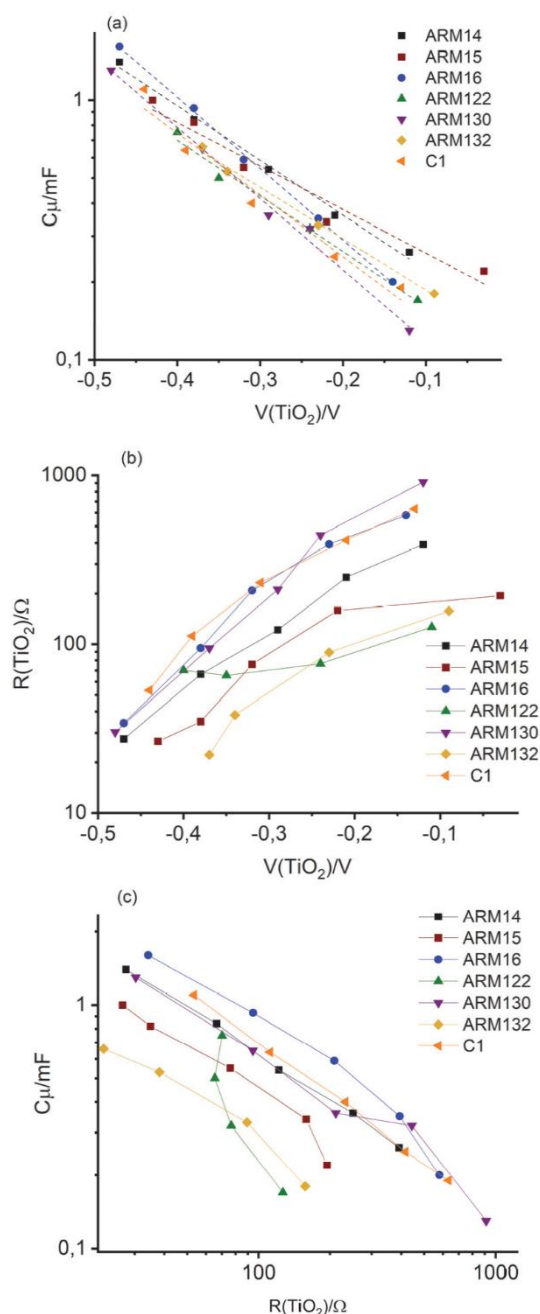


Figure 7: TiO_2 (a) capacitance and (b) recombination resistance of Fe(II)NHC plotted vs V_{TiO_2} . (c) Chemical Capacitance vs recombination Resistance of the TiO_2 .

This potential region should be dominated by the chemical capacitance of the titania film and by its interfacial recombination resistance R_{TiO_2} which result in one dominant depressed semicircle in the Nyquist plots (Figure S53). Fitting of the EIS data was accomplished with both the transmission line elaborated by Bisquert et al.^[35] (Figure S53h) and with a simpler model (Figure S54a) consisting of two RC meshes

accounting for the electrochemical interfaces of the photoanode and the counter electrode respectively. In general, with both models, a short Warburg element was introduced in order to account for electrolyte diffusion in the thin layer cell, giving rise to a further low frequency feature in the complex plane plots. The transmission line model was mostly useful to fit the EIS response at intermediate forward voltage values ($-0.25/-0.3\text{V}$) where the transport resistance is not entirely negligible compared to the recombination resistance of the TiO_2 (R_{TiO_2}). However, the recombination resistance varies in the range of 10^3 - 10^1 and is dominant over the transport resistance by a factor of at least 10 explaining the substantial agreement between the two models, particularly when the open circuit voltage is progressively approached. In all cases the sum of the resistances extracted from fits display an excellent agreement with the reciprocal derivative $\partial V/\partial i$ of the i/V curves (Figure S55) validating the models and their correspondence with the cell elements responsible with photocurrent generation. Figure 7a and Figure S54 reports in the ordinate log scale the chemical capacitance^[36] of the sensitized titania film (C_{μ}), as a function of V_{TiO_2} where $V_{\text{TiO}_2} = V_{\text{cell}} - I \sum R$ where I is the photocurrent and $\sum R$ is the sum of the resistances due to other cell components. C_{μ} decreases exponentially by decreasing the applied forward voltage.

All the FeSSCs display at comparable V_{TiO_2} values a similar range of photoanodic capacitance, which is originated by the steady state electronic population of TiO_2 at each given voltage, determined by the competition between charge injection and recombination. Figure 7b shows $\log R_{\text{TiO}_2}$ vs V_{TiO_2} . The recombination resistance decreases with increasing chemical capacitance of the titania film which reflects in an improved electronic conductivity of the latter. The C_{μ} vs R_{TiO_2} is informative about the recombination dynamics in the cell, allowing to compare the recombination resistance at a comparable value of electronic population of the semiconductor. In principle, the best performing systems should couple the highest chemical capacitance with the largest recombination resistance, which means that we can realize the most favorable competition of charge separation against electron recombination. From the $\log C_{\mu}/\log R_{\text{TiO}_2}$ plot in Figure 7c we observed the best behavior with dyes **ARM16**, **ARM14** and **ARM130** while **ARM122** and **ARM132** display the lowest recombination resistance, consistent with the lower V_{oc} (< 0.4 V) recorded when using these latter dyes. We can state that the best performance of **ARM130** seems to result from of an ideal combination of the best injection efficiency and light harvesting, while the recombination dynamics are not dramatically different from those of the other dyes bearing aromatic substituents.

Charge transfer at the ARM130@ TiO_2 interface

To get deeper insights on the effect of the chemical substitution in the best **ARM130** sensitizer on the interfacial charge injection and recombination properties, here we have modelled the ARM130@ TiO_2 interface (Figure 8a) and calculated its energetics (Figure 8b), injection and recombination kinetics (Table 4 and Table S7, respectively). Here we will compare the data with those obtained for the unsubstituted **ARM13** compound^[20] to check if the presence of a substituent on the ancillary NHC ligand effectively induces an improvement in the interfacial electron/transfer kinetics. It is important to stress that here we do not consider the presence of the Mg^{2+} cation at the

interface, that, as we have already discussed in our previous work,^[20] is going to systematically increase the interfacial electronic coupling, without acting in a differential way on the two dyes, thus allowing us to still draw reliable conclusions. The relaxed structure of **ARM130** anchored on the TiO₂ slab (Figure 8a) shows a rather pronounced bending of the dye toward the metal oxide surface (displaying tilted angles θ about 47°), as already found for other NHC-Fe(II) complexes.^[37,20] The O-Ti covalent bonds are in the range 2.10-2.20 Å, typical values for carboxylic acid groups anchoring to TiO₂ surfaces (see Table S8).

Table 4: Probability Distributions, $\Gamma_{inj}(\epsilon)$ (eV) and DOS (number of states/eV) calculated at the diabatic LUMO energies and associated Injection times, τ_{inj} (s⁻¹). The diabatic TiO₂ conduction band maximum (CBM) is also reported.

System	Dye LUMO (eV)	CBM (eV)	TiO ₂ DOS (states/eV)	Γ_{inj} (eV)	τ_{inj} (fs)
ARM130@TiO ₂	-2.51	-3.32	13962	0.150	4.39
ARM13@TiO ₂ ^[a]	-2.60	-3.34	12651	0.152	4.33

^[a] Data taken from Ref.22

The interfacial electronic structure, evidenced by the Projected Density of States (PDOS) in Figure 8b, shows a favourable energy level alignment and a notable broadening of the dye's LUMO over the TiO₂ conduction band (CB) states, which, indeed, qualitatively account for the good injection performances measured for this complex.

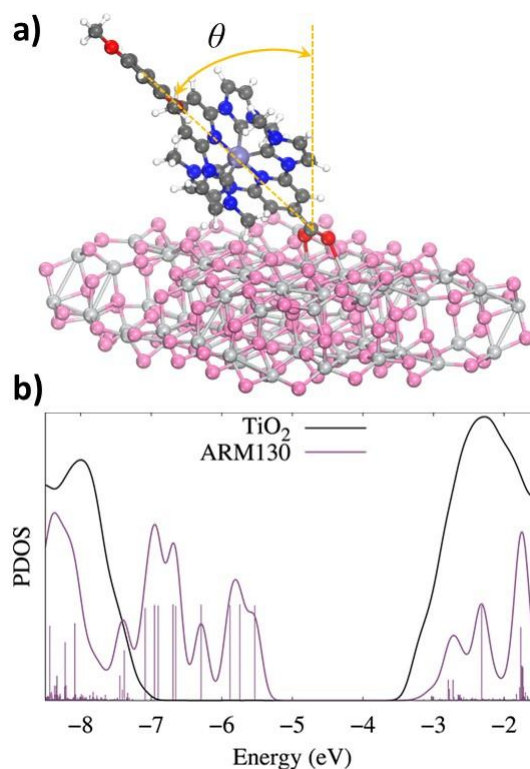


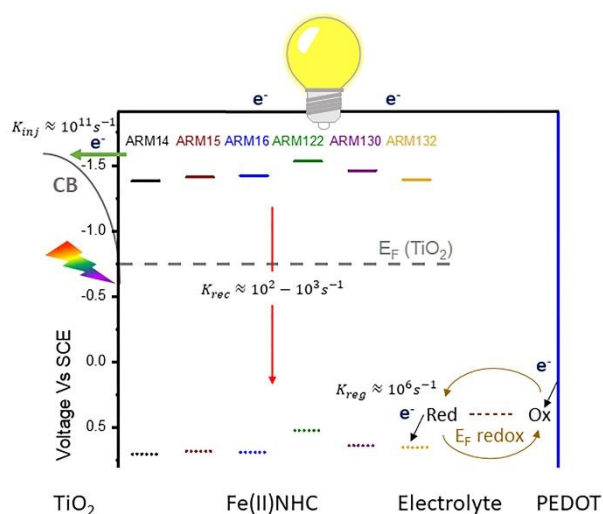
Figure 8: a) Perspective view of the optimized **ARM130@TiO₂** structure; and b) Projected Density of States (PDOS) of **ARM-130@TiO₂** over the atoms belonging to the dye (purple) and TiO₂ surface (black), as calculated by Mulliken population analysis. For visualisation purposes, only the vertical bars of the dye's PDOS are represented here and the TiO₂ DOS intensity has been divided by a factor of 10.

By looking at data in Table 4, we can quantitatively assess the differences in the electron injection kinetics of **ARM130@TiO₂** and **ARM13@TiO₂**. The diabatic LUMO of **ARM130** is up shifted of about 0.1 eV with respect to the LUMO of **ARM13**, thus lying more deeply in the TiO₂ CB, as indicated by the larger number of semiconductor states (ca. 14000 vs. 12600). This LUMO up shift in **ARM130** basically compensates the slightly lower electronic coupling with the TiO₂ states around the LUMO energy level (Figure S56), finally yielding injection properties (Γ_{inj} and τ_{inj}) similar to those calculated for the unsubstituted **ARM13** complex. Analogously, comparable back electron recombination kinetics are also predicted (Table S7). Therefore, this chemical substitution on the ancillary ligand does not seem to significantly affect the interfacial charge generation properties.

Based on this analysis, we can, therefore, attribute the record photovoltaic performances, i.e., the record photocurrent, of **ARM130** to the effect of electron donating OMe groups attached to the benzene ring, which improve the light harvesting capability without deteriorating the excited directionality, as it was the case, instead, of **ARM15**.

Conclusion

Figure 9: Energy levels of the Fe(II) based DSSC explored in this work with



time constants of injection, charge separation and recombination.

This work is an important accomplishment in the quest for abundant-metal based solar cells. We report here a record power conversion efficiency of 1.83%, never recorded for a Fe-sensitized DSSC. To reach such an unprecedented performance, we designed a new family of six heteroleptic complexes bearing functionalities with different electronic properties with the aim to improve the charge separation as well of light harvesting in these dyes. In figure 9 are summarized the energy levels of the new sensitizers and the different time constants of the processes at play in the corresponding FeSSCs all being favorable to efficient cell operating.

Among all dyes investigated, **ARM130** bearing a dimethoxyphenyl group on the ancillary ligand was found the most efficient of the series. Computational modelling and electrochemical impedance spectroscopy analyses converge towards the conclusion that this dye combines an improved light harvesting capability induced by electron donating OMe groups attached to the benzene ring and favorable excited directionality and recombination kinetics. The efficiency was also optimized by using Mg^{2+} /TBAI-based electrolyte as well as a thick TiO_2 photoanode.

Here we demonstrate that the performances of Iron-based DSSCs can be notably boosted by the development of thorough synthesis-computation-characterization investigations allowing to explain and improve the efficiency of the photoinduced interfacial electron transfer processes.

Acknowledgements

The L2CM thanks the French Agence Nationale de Recherche (ANR-16-CE07-0013-02), Lorraine Université d'Excellence (IMPACT N4S) and the European Regional Development Funds (Programme opérationnel FEDER-FSE Lorraine et Massif des Vosges 2014-2020/"Fire Light" project: "Photo-bio-active molecules and nanoparticles" for financial support and grants to A.R.M. The L2CM laboratory is also grateful to F. Dupire for mass spectrometry of the

complexes. University of Ferrara acknowledges financial support from Emilia Romagna Region and H2020 Research Innovation Actions 2020-2024 „CONDOR“. This project has received funding from the European Union's Horizon 2020 research and innovation programme under grant agreement No 101006839. The LPCT thanks the European Regional Development Funds (Programme opérationnel FEDER-FSE Lorraine et Massif des Vosges 2014-2020/ COMETE project: „COnception in silico de Matériaux pour l'Environnement et l'Energie“ for financial support to V. D-C.

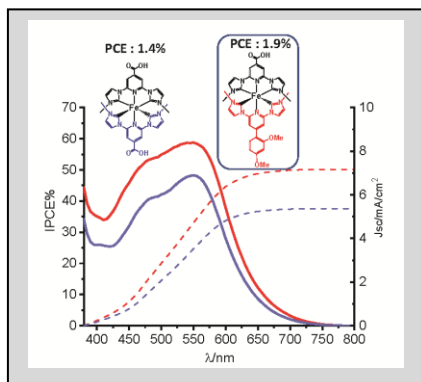
Keywords: iron complexes • NHC• sensitizers • light harvesting • DSSC

References

- [1] K. E. Dalle, J. Waman, J. J. Leung, B. Reuillard, I. S. Karmel, E. Reiser, *Chem. Rev.* **2019**, *119*, 2752–2875.
- [2] C. A. Bignozzi, R. Argazzi, R. Boaretto, E. Busatto, S. Carli, F. Ronconi, S. Caramori, *Coord. Chem. Rev.* **2013**, *257*, 1472–1492.
- [3] A. Zamora, G. Viguera, V. Rodríguez, M. D. Santana, J. Ruiz, *Coord. Chem. Rev.* **2018**, *360*, 34–76.
- [4] T. Duchanois, L. Liu, M. Pastore, A. Monari, C. Cebrián, Y. Trolez, M. Darari, K. Magra, A. Francés-Monerris, E. Domenichini, M. Beley, X. Assfeld, S. Haacke, P. Gros, *Inorganics* **2018**, *6*, 63.
- [5] S. Ferrere, B. A. Gregg, *J. Am. Chem. Soc.* **1998**, *120*, 843–844.
- [6] S. Ferrere, *Chem. Mater.* **2000**, *12*, 1083–1089.
- [7] J. E. Monat, J. K. McCusker, *J. Am. Chem. Soc.* **2000**, *122*, 4092–4097.
- [8] G. Auböck, M. Chergui, *Nat. Chem.* **2015**, *7*, 629–633.
- [9] A. L. Smeigh, M. Creelman, R. A. Mathies, J. K. McCusker, *J. Am. Chem. Soc.* **2008**, *130*, 14105–14107.
- [10] M. Cammarata, R. Bertoni, M. Lorenc, H. Cailleau, S. Di Matteo, C. Mauriac, S. F. Matar, H. Lemke, M. Chollet, S. Ravy, C. Lauthé, J.-F. Létard, E. Collet, *Phys. Rev. Lett.* **2014**, *113*, 227402.
- [11] Y. Liu, T. Harlang, S. E. Canton, P. Chábera, K. Suárez-Alcántara, A. Fleckhaus, D. A. Vithanage, E. Göransson, A. Corani, R. Lomoth, V. Sundström, K. Wärnmark, *Chem. Commun.* **2013**, *49*, 6412.
- [12] L. Liu, T. Duchanois, T. Etienne, A. Monari, M. Beley, X. Assfeld, S. Haacke, P. C. Gros, *Phys Chem Chem Phys* **2016**, *18*, 12550–12556.
- [13] M. Darari, E. Domenichini, A. Francés-Monerris, C. Cebrián, K. Magra, M. Beley, M. Pastore, A. Monari, X. Assfeld, S. Haacke, P. C. Gros, *Dalton Trans.* **2019**, *48*, 10915–10926.
- [14] K. Magra, E. Domenichini, A. Francés-Monerris, C. Cebrián, M. Beley, M. Darari, M. Pastore, A. Monari, X. Assfeld, S. Haacke, P. C. Gros, *Inorg. Chem.* **2019**, *58*, 5069–5081.
- [15] K. Magra, M. Darari, E. Domenichini, A. Francés-Monerris, C. Cebrián, M. Beley, M. Pastore, A. Monari, X. Assfeld, S. Haacke, P. C. Gros, *J. Phys. Chem. C* **2020**, *124*, 18379–18389.
- [16] M. Bauer, J. Steube, A. Pápcke, O. Bokareva, T. Reuter, S. Demeshko, R. Schoch, S. Hohloch, F. Meyer, K. Heinze, O. Kühn, S. Lochbrunner, *Janus-Type Dual Emission of a Cyclometalated Iron(III) Complex*, In Review, **2020**.
- [17] C. D. Clark, M. Z. Hoffman, D. Paul Rillema, Q. G. Mulazzani, *J. Photochem. Photobiol. Chem.* **1997**, *110*, 285–290.
- [18] T. Duchanois, T. Etienne, C. Cebrián, L. Liu, A. Monari, M. Beley, X. Assfeld, S. Haacke, P. C. Gros, *Eur. J. Inorg. Chem.* **2015**, *2015*, 2469–2477.
- [19] E. Marchini, M. Darari, L. Lazzarin, R. Boaretto, R. Argazzi, C. A. Bignozzi, P. C. Gros, S. Caramori, *Chem. Commun.* **2020**, *56*, 543–546.
- [20] A. Reddy Marri, E. Marchini, V. D. Cabanes, R. Argazzi, M. Pastore, S. Caramori, P. C. Gros, *J. Mater. Chem. A* **2021**, *9*, 3540–3554.
- [21] H. Abe, H. Kurokawa, Y. Chida, M. Inouye, *J. Org. Chem.* **2011**, *76*, 309–311.
- [22] M. Schlosser, C. Bobbio, T. Rausis, *J. Org. Chem.* **2005**, *70*, 2494–2502.

-
- [23] T. Duchanois, T. Etienne, C. Cebrián, L. Liu, A. Monari, M. Beley, X. Assfeld, S. Haacke, P. C. Gros, *Eur. J. Inorg. Chem.* **2015**, 2015, 2469–2477.
- [24] R. L. Martin, *J. Chem. Phys.* **2003**, 118, 4775–4777.
- [25] F. Plasser, *J. Chem. Phys.* **2020**, 152, 084108.
- [26] Y. Tachibana, J. E. Moser, M. Grätzel, D. R. Klug, J. R. Durrant, *J. Phys. Chem.* **1996**, 100, 20056–20062.
- [27] S. E. Koops, B. C. O'Regan, P. R. F. Barnes, J. R. Durrant, *J. Am. Chem. Soc.* **2009**, 131, 4808–4818.
- [28] T. D. Santos, A. Morandeira, S. Koops, A. J. Mozer, G. Tsekouras, Y. Dong, P. Wagner, G. Wallace, J. C. Earles, K. C. Gordon, D. Officer, J. R. Durrant, *J. Phys. Chem. C* **2010**, 114, 3276–3279.
- [29] A. Reddy Marri, E. Marchini, V. D. Cabanes, R. Argazzi, M. Pastore, S. Caramori, P. C. Gros, *J. Mater. Chem. A* **2021**, 9, 3540–3554.
- [30] E. Marchini, M. Darari, L. Lazzarin, R. Boaretto, R. Argazzi, C. A. Bignozzi, P. C. Gros, S. Caramori, *Chem. Commun.* **2020**, 56, 543–546.
- [31] Y. Ma, S. R. Pendlebury, A. Reynal, F. Le Formal, J. R. Durrant, *Chem Sci* **2014**, 5, 2964–2973.
- [32] S. Ardo, Y. Sun, F. N. Castellano, G. J. Meyer, *J. Phys. Chem. B* **2010**, 114, 14596–14604.
- [33] J. R. Durrant, S. A. Haque, E. Palomares, *Coord. Chem. Rev.* **2004**, 248, 1247–1257.
- [34] S. Ardo, Y. Sun, A. Staniszewski, F. N. Castellano, G. J. Meyer, *J. Am. Chem. Soc.* **2010**, 132, 6696–6709.
- [35] F. Fabregat-Santiago, J. Bisquert, G. Garcia-Belmonte, G. Boschloo, A. Hagfeldt, *Sol. Energy Mater. Sol. Cells* **2005**, 87, 117–131.
- [36] J. Bisquert, *Phys. Chem. Chem. Phys.* **2003**, 5, 5360.
- [37] M. Pastore, T. Duchanois, L. Liu, A. Monari, X. Assfeld, S. Haacke, P. C. Gros, *Phys. Chem. Chem. Phys.* **2016**, 18, 28069–28081.
- [38] G. Di Carlo, S. Caramori, V. Trifiletti, R. Giannuzzi, L. De Marco, M. Pizzotti, A. Orbelli Biroli, F. Tessore, R. Argazzi, C. A. Bignozzi, *ACS Appl. Mater. Interfaces* **2014**, 6, 15841–15852.
- [39] E. Marchini, S. Caramori, R. Boaretto, V. Cristino, R. Argazzi, A. Nioiretini, C. A. Bignozzi, *Appl. Sci.* **2021**, 11, 2769.
- [40] S. Carli, E. Busatto, S. Caramori, R. Boaretto, R. Argazzi, Cliff. J. Timpson, C. A. Bignozzi, *J. Phys. Chem. C* **2013**, 117, 5142–5153.
- [41] M. Reiher, O. Salomon, B. Artur Hess, *Theor. Chem. Acc. Theory Comput. Model. Theor. Chim. Acta* **2001**, 107, 48–55.
- [42] L. A. Fredin, M. Pápai, E. Rozsályi, G. Vankó, K. Wärnmark, V. Sundström, P. Persson, *J. Phys. Chem. Lett.* **2014**, 5, 2066–2071.
- [43] I. M. Dixon, F. Alary, M. Boggio-Pasqua, J.-L. Heully, *Dalton Trans.* **2015**, 44, 13498–13503.
- [44] K. P. Kepp, *Inorg. Chem.* **2016**, 55, 2717–2727.
- [45] J. Tomasi, B. Mennucci, R. Cammi, *Chem. Rev.* **2005**, 105, 2999–3094.
- [46] **N.d.**
- [47] M. Pastore, T. Duchanois, L. Liu, A. Monari, X. Assfeld, S. Haacke, P. C. Gros, *Phys Chem Chem Phys* **2016**, 18, 28069–28081.
- [48] J. P. Perdew, K. Burke, M. Ernzerhof, *Phys. Rev. Lett.* **1997**, 78, 1396–1396.
- [49] A. Klamt, G. Schüürmann, *J Chem Soc Perkin Trans 2* **1993**, 799–805.
- [50] S. Grimme, J. Antony, S. Ehrlich, H. Krieg, *J. Chem. Phys.* **2010**, 132, 154104.
- [51] G. te Velde, F. M. Bickelhaupt, E. J. Baerends, C. Fonseca Guerra, S. J. A. van Gisbergen, J. G. Snijders, T. Ziegler, *J. Comput. Chem.* **2001**, 22, 931–967.
- [52] I. Kondov, M. Čížek, C. Benesch, H. Wang, M. Thoss, *J. Phys. Chem. C* **2007**, 111, 11970–11981.
- [53] W. Yao, S. Das, N. A. DeLucia, F. Qu, C. M. Boudreaux, A. K. Vannucci, E. T. Papish, *Organometallics* **2020**, 39, 662–669.

Entry for the Table of Contents



A Fe(II)NHC sensitizer bearing a dimethoxyphenyl group on the ancillary ligand scored the highest efficiency ever reported for an iron-sensitized solar cell (1.83%) using Mg^{2+} and NBu_4I -based electrolyte and a thick $20\mu m$ TiO_2 anode.

Institute and/or researcher Twitter usernames: @L2CM_UMR7053